

The effect of the TiC particle size on the preferred oxidation temperature for self-healing of oxide ceramic matrix materials

Boatema, L.; Brouwer, Hans; van der Zwaag, S.; Sloof, W. G.

DOI

[10.1007/s10853-017-1973-x](https://doi.org/10.1007/s10853-017-1973-x)

Publication date

2018

Document Version

Final published version

Published in

Journal of Materials Science

Citation (APA)

Boatema, L., Brouwer, H., van der Zwaag, S., & Sloof, W. G. (2018). The effect of the TiC particle size on the preferred oxidation temperature for self-healing of oxide ceramic matrix materials. *Journal of Materials Science*, 53(8), 5973-5986. <https://doi.org/10.1007/s10853-017-1973-x>

Important note

To cite this publication, please use the final published version (if applicable). Please check the document version above.

Copyright

Other than for strictly personal use, it is not permitted to download, forward or distribute the text or part of it, without the consent of the author(s) and/or copyright holder(s), unless the work is under an open content license such as Creative Commons.

Takedown policy

Please contact us and provide details if you believe this document breaches copyrights. We will remove access to the work immediately and investigate your claim.



The effect of the TiC particle size on the preferred oxidation temperature for self-healing of oxide ceramic matrix materials

L. Boatemaa^{1,*} , J. C. Brouwer¹, S. van der Zwaag², and W. G. Sloof¹

¹Department of Materials Science and Engineering, Delft University of Technology, Mekelweg 2, 2628 CD Delft, The Netherlands

²Faculty of Aerospace Engineering, Delft University of Technology, Kluyverweg 1, 2629 HS Delft, The Netherlands

Received: 29 September 2017

Accepted: 27 December 2017

© The Author(s) 2018. This article is an open access publication

ABSTRACT

The effect of particle size on the oxidation kinetics of TiC powders is studied. Different sizes of TiC powder ranging from nanometre to submillimetre sizes are investigated. The samples are heated at different heating rates from room temperature up to 1200 °C in dry synthetic air. The Kissinger method for analysis of non-isothermal oxidation is used to estimate the activation energy for oxidation of the powders and to identify the active temperature window for efficient self-healing. The master curve plotting method is used to identify the model which best describes the oxidation of TiC powders, and the Senum and Yang method is used to approximate the value for the Arrhenius constant. The oxidation of TiC proceeds via the formation of oxycarbides, anatase and then finally the most stable form: rutile. The activation energy is found to be a strong function of the particle size for particle sizes between 50 nm and 11 µm and becomes constant at larger particle sizes. The data demonstrate how the minimal healing temperature for oxide ceramics containing TiC as healing particles can be tailored between 400 and 1000 °C by selecting the right average TiC particle size.

Introduction

Embedded titanium carbide (TiC) particles are being considered as a potential healing agent to autonomously repair crack damage in oxide ceramics used in high-temperature applications [1]. For such (extrinsic) self-healing ceramics, microscopic cracks in the material will also intersect the sacrificial healing particle and allow atmospheric oxygen to reach it.

The local supply of oxygen via the open cracks to the intersected TiC particles will cause them to oxidize, leading to the formation of TiO₂ which both fills the crack and adheres strongly to the faces of the crack [2]. Hence, the so-called healing reaction leads to a partial or complete recovery of the mechanical properties of the material and an extension of the lifetime of the component. To be a successful strategy, it is important that the oxidation reaction takes

Address correspondence to E-mail: l.boatemaa@tudelft.nl

place at the prevailing conditions (in particular the right temperature) and with the right kinetics. A general analysis of the required properties of the healing particles leading to autonomous self-healing at high temperature can be found in [2].

However, the cited analysis did not specify the minimal temperature window required to trigger the healing reaction. Of course, the required minimal temperature to trigger the healing reaction depends primarily on the chemical stability of the healing material in an oxygen-containing environment. This dependence has already been demonstrated (but apparently not been appreciated) in the combined first-generation studies on self-healing of Al_2O_3 or Si_3N_4 filled with SiC or Ni particles [3–7]. In these studies, the crack healing ability was studied as a function of both temperature (from 900 to 1400 °C) and time (between 1 and 300 h) and widely different values were obtained for different particle sizes.

While the optimal healing temperature has been shown to vary significantly with the chemical composition of the healing particle and to a lesser degree of that of the matrix material, very few studies, with the exception of [8], performed a systematic study on the effect of particle size on the healing kinetics given a fixed composition for both the particle and the matrix. In their study, Nakao and Abe [8] measured the strength recovered by high-temperature oxidation of alumina containing 18 vol% SiC particles of size 270, 30 and 10 nm. They reported that reducing the size of SiC reduced the oxidation/healing temperature from 1200 to 950 °C, due to the faster oxidation kinetics at lower particle sizes.

Recently, the ability of 2- μm -sized TiC particles to heal surface cracks in alumina has been studied by Yoshioka et al. [1]. Healing of two different composites containing 15 and 30 vol% of TiC was studied as a function of temperature ranging from 400 to 800 °C in air and a fixed time of 1 h. Full strength was obtained for a composite containing 30 vol% of TiC upon annealing in air at 800 °C for 1 h. Also, in situ healing of these alumina composites was demonstrated [9]. Surface cracks were healed when the material was exposed in a combustion chamber with a high-velocity exhaust gas mixture at approx. 1000 °C and a low oxygen partial pressure.

The oxidation behaviour of bulk TiC has already been investigated as a function of temperature (from 600 to 1200 °C) and oxygen partial pressure (13–100 kPa) [10, 11]. The observable trend in these

studies is that oxidation proceeds parabolically from 600 to 800 °C and switches to linear kinetics at higher temperatures and higher oxygen partial pressures. Four steps were identified during the transformation of TiC powders to TiO_2 [12, 13]. The first step involves the substitution of atomic oxygen for the carbon present at the interstitial vacancies of the TiC lattice leading to the formation of the oxycarbides/titanium suboxide layer. In the next step, the titanium suboxides oxidise into amorphous titanium dioxide and further crystallize to anatase. In third stage, the crystallization of anatase continues and the resulting volume expansion leads to the cracking of the oxide layers, and this provides fast short-circuit diffusion paths oxidation. In the fourth and final step, anatase is formed continuously and rather rapidly transformed into rutile. The rate-determining step is the diffusion of oxygen through the already formed oxide layers.

With TiC having been identified as a potential healing agent for alumina [2], the current work focusses on the determination of the effect of TiC particle size on its oxidation kinetics in order to explore the possibility to lower the minimal healing temperature of alumina containing TiC to temperatures below 1000 °C. To this aim, differential thermal and thermogravimetric analyses are performed for TiC powders of different particle sizes over the temperature range from room temperature to 1200 °C. The kinetic triplet, i.e. the activation energy, the reaction model and the Arrhenius constant, is determined for all powders and such information, in principle, allows the prediction of the optimal healing temperature for any inert ceramic containing TiC particles as the discrete, extrinsic healing agent.

Analysis of reactions

In solid–gas reactions, the solid phase is usually a granular medium through which the gaseous reactant circulates and reacts at the solid interface [14]. Due to the reactions occurring at a microscopic level, the solid material undergoes chemical and structural change as the reaction proceeds. Several reaction models are used in describing gas–solid reactions [15]. The unreacted shrinking core model is commonly used. In this model, the reaction product forms a solid layer that allows diffusion of reactant gas towards the interface between the product layer

and unreacted core. A continuous reaction leads to the advancing of a reaction front, or equivalently, a shrinking core. The entire reaction kinetics involves three steps: transport and dissolution of the gas reactant at the solid surface, diffusion of the gas reactant through the product layer towards the unreacted core and finally chemical reaction of the gas with the solid reactant at the product–core interface [16].

Thermal analysis is employed to study the heterogeneous reactions. In (simultaneous) differential thermal analysis (DTA), the heat flow and, in thermogravimetric analysis (TGA), the mass change are measured while the material is heated at a constant the heating rate [17]. From the measured data, the kinetic triplet, which describes the conversion of a material (α) as a function of temperature (T) and time (t), is derived. The kinetic triplet parameters are the activation energy E_A , the Arrhenius or frequency constant A and the reaction model $f(\alpha)$ [18]. For non-isothermal experiments, the rate of transformation of any material is given by:

$$\frac{d\alpha}{dT} = \frac{d\alpha}{dt} \cdot \frac{dt}{dT} \tag{1}$$

where the fraction converted at any time is given by:

$$\alpha = \frac{m_t - m_0}{m_\infty - m_0} \tag{2}$$

in which m_0 , m_t and m_∞ denote the mass at time t 0, t and ∞ (i.e. after full conversion), respectively. dT/dt is the heating rate denoted as β , and $d\alpha/dt$ is the isothermal conversion rate and expressed as:

$$\frac{d\alpha}{dt} = A e^{-\frac{E_A}{RT}} f(\alpha) \tag{3}$$

Combining Eqs. (1) and (3) leads to the non-isothermal conversion rate:

$$\frac{d\alpha}{dT} = \frac{A}{\beta} e^{-\frac{E_A}{RT}} f(\alpha) \tag{4}$$

Integration results in the non-isothermal transformation rate law given by:

$$g(\alpha) = \frac{A}{\beta} \int_0^T e^{-\frac{E_A}{RT}} dT \tag{5}$$

This temperature integral has no analytical solution [17, 19], but is usually approximated by a series expansion or converted in an approximate form that can be integrated. A frequently used approximation

is that by Senum and Yang [20]. Consider $x = E_A/RT$, then:

$$\int_0^T e^{\frac{E_A}{RT}} dT = \frac{E_A}{R} \int_x^\infty \frac{e^{-x}}{x^2} dx \tag{6}$$

With $p(x) = \int_x^\infty \frac{e^{-x}}{x^2} dx$, Eq. (6) is approximated with the fourth rational of Senum and Yang [20], i.e.

$$p(x) = \frac{e^{-x}}{x} \left[\frac{x^3 + 18x^2 + 86x + 96}{x^4 + 20x^3 + 120x^2 + 240x + 120} \right] \tag{7}$$

Successively, the activation energy, the reaction model and finally the Arrhenius constant will be determined from non-isothermal experimental data. In the above analysis, the kinetic parameters are considered to be independent of temperature and fraction converted.

Activation energy

Regardless of the reaction order, the activation energy of the conversion reaction E_A can be obtained directly from non-isothermal TGA or DTA data using the so-called Kissinger method [21, 22]. If the temperature rises during the reaction, the reaction rate will rise to a maximum value, but return to zero as the reactant is exhausted. The maximum rate is associated with either a maximum mass change or heat evolution, which occurs at the peak temperature. Then, the governing equation for the determination of the activation energy reads:

$$\ln \left(\frac{\beta}{T_p^2} \right) + \frac{E_A}{RT_p} = C \tag{8}$$

where T_p is the peak temperature, corresponding to the temperature at which the reaction rate is at maximum. Then, the highest heat flux or mass change rate is recorded. R is the gas constant, and C is a constant. Thus, the activation energy (E_A) is obtained by plotting $\ln(\beta/T_p^2)$ versus $1/T_p$ for a series of measurements at different heating rates β .

Reaction model

The reaction model mathematically describes the conversion process of a material as a result of an occurring chemical or physical reaction. Different models have been derived for solid-state reactions [18], which comprises nucleation, geometrical contraction, diffusion and reaction-order models. To

determine the appropriate model to analyse the experimental data, the so-called master curve plotting method is used. This method is based on the concept of generalized time θ [23], which is defined by Eq. (9) for isothermal or non-isothermal reactions, respectively, as:

$$\theta = \int_0^t e^{\frac{-E_A}{RT}} dt \text{ or } \theta = \frac{1}{\beta} \int_0^T e^{\frac{-E_A}{RT}} dT \quad (9)$$

θ denotes the reaction time taken to attain a particular fraction converted at infinite temperature. Now, Eqs. (3) and (5) can be rewritten in terms of generalized time, respectively, as:

$$\frac{dx}{d\theta} = Af(\alpha) \quad (10)$$

$$g(\alpha) = A\theta \quad (11)$$

As a reference point for the master curve plotting analysis, generally the level $\alpha = 0.5$ is chosen and using Eq. (10) it can be derived that:

$$\frac{d\alpha/d\theta}{(d\alpha/d\theta)_{\alpha=0.5}} = \frac{f(\alpha)}{f(0.5)} \quad (12)$$

From the experimentally determined conversion rate, with respect to the generalized time, as a function of fraction converted, $f(\alpha)/f(0.5)$ versus α can be obtained, since

$$\frac{dx}{d\theta} = \frac{dx}{dt} \exp\left(\frac{E_A}{RT}\right) \text{ or } \frac{dx}{d\theta} = \beta \frac{dx}{dT} \exp\left(\frac{E_A}{RT}\right) \quad (13)$$

By comparing the experimental result with theoretical reaction models [23], the reaction model that best fits the measured data can be determined. From this, the key reaction mechanisms can be determined and this knowledge can be used to optimise the material performance.

Arrhenius constant

The last of the kinetic triplet, i.e. the pre-exponential factor (A), can be evaluated from Eq. (11), once the reaction model is determined; cf. "Reaction model" section. The generalized time θ for non-isothermal reactions [Eq. (9)] resembles Eq. (6) and hence can be written as:

$$\theta = \frac{E_A}{\beta R} p(x) \quad (14)$$

while $p(x)$ is approximated using Eq. (7).

Experimental procedure

The five TiC powders used in this study are all commercially available, and their main features are summarized in Table 1. The first and second powders, having an average particle size of 140 and 48 μm , respectively, were obtained by sieving a TiC powder with a broad size distribution (Goodfellow, UK; product number TI546030). The third TiC powder with an average particle size of 5 μm was supplied by Alfa Aesar, Germany (product number TiC 40178). The fourth TiC powder with an average particle size of 0.8 μm was supplied by American Elements, USA (product number TI-C-03M-NP.800NS). Finally, the fifth TiC powder with an average particle size of 50 nm was supplied by Chempur, Germany (Product number CFF-NP059).

The purity of the powders studied was determined with X-ray fluorescence spectroscopy (XRF) using an Axios Max WD-XRF instrument (PANanalytical, The Netherlands), and the data were evaluated with SuperQ5.0i/Omnian software. The size distribution of the TiC particles was determined by laser diffraction using the Microtrac 3500 (Microtrac Inc., USA) equipped with a tri-laser diode detection system. The particle morphology of each TiC powder was recorded with scanning electron microscopy (SEM) using a JSM 6500F (JEOL, Japan). The instrument used was equipped with an energy-dispersive spectrometer (EDS; Ultra Dry 30 mm² detector, Thermo Fisher Scientific, USA) for X-ray microanalysis (XMA).

The oxidation kinetics of the TiC powders was studied non-isothermally using simultaneous thermogravimetric (TG) and differential thermal analysis (DTA) using a high-performance symmetrical double furnace balance (TAG 16/18, Setaram, France). 20 ± 1 mg of the powder was put into a 100- μL Al₂O₃ crucible and placed onto a TG-DTA rod with an S-type thermocouple. A similar rod but without crucibles was placed as a counterweight on the other side of the balance to aid automatic correction of buoyancy effects. Then, the dual furnaces were heated up from room temperature to 1200 °C with various heating rates (between 1 and 10 °C min⁻¹). In each measurement, both furnaces were purged with dry synthetic air (N₂ + 20 vol% O₂ and H₂O < 10 ppm) at a total flow rate of 50 sccm. The evolved gas at the sample location was collected and analysed with an Omnistar GSD 301 system having a quadrupole mass spectrometer (QMS 200 M3 from Pfeiffer

Table 1 Size and composition of TiC powders with D_{50} as the average particle size and D_{10} and D_{90} as the particle size at 10 and 90% cut-off, respectively, in the size distribution

Powder	D_{50} (μm)	D_{10} – D_{90} (μm)	TiC (wt%)	Main impurities (wt%)
1	140	100–150	99.75	Fe 0.089 Si 0.04
2	48	40–50	99.75	Fe 0.089 Si 0.04
3	5	2–15	98.17	WC 1.552 Fe 0.105
4	0.8	0.6–1	90.8	W 7.25 Co 0.68
5	0.05	0.04–0.07	99.966	Si 0.017 Cl 0.008

Omnistar, Germany) in order to observe the evolution of CO_2 .

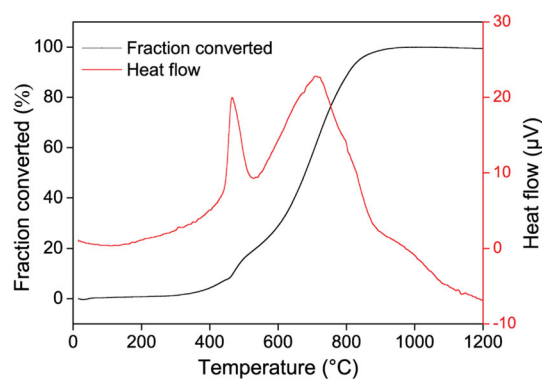
The thermal analysis system used was equipped with Calisto acquisition and processing software (v1.43 DB v1.44, Setaram, France) which records both the furnace and the sample temperature. For accurate results, the temperature measured by the thermocouples at the sample position is used for the analysis as this represents the true sample temperature. Prior to admitting the gases to the furnaces, each gas, i.e. Ar, N_2 and O_2 (all with 5 N vol% purity), was filtered to remove any residual hydrocarbons, moisture and oxygen (for N_2 and Ar). The Accosorb (< 10 ppb hydrocarbons), Hydrosorb (< 10 ppb H_2O) and Oxysorb (< 5 ppb O_2) filters (Messer Griesheim, Germany) were used. The flow of each gas was regulated and monitored with LabView (version 12, National Instruments, USA) using calibrated mass flow controllers (Bronkhorst, The Netherlands).

The oxidation products and lattice parameter were identified and measured by X-ray diffraction using a Bruker D8 Advance diffractometer (Bruker, Germany) equipped with a graphite monochromator. Diffractograms were recorded with Co $\text{K}\alpha$ radiation in the 2θ range of 10° – 130° and a step size of 0.034° . The data were processed with the Diffrac EVA 4.1 Bruker software.

Results

TiC powder oxidation

Oxidation of the 5 μm powder was studied first by heating from room temperature to 1200 $^\circ\text{C}$ at 5°C min^{-1} in air, and the heat flow and the conversion curves are presented in Fig. 1. Transformation

**Figure 1** Heat flow and mass gained signals for the 5 μm powder oxidized at 5°C min^{-1} in dry synthetic air.

starts just before 400 $^\circ\text{C}$ and ends around 900 $^\circ\text{C}$ via two exothermic peaks at about 470 and 710 $^\circ\text{C}$. Therefore, to fully describe the oxidation of TiC, two separate experiments are performed on the same powder under the same conditions till the end of each peak (i.e. till 530 and 900 $^\circ\text{C}$) and the oxidation products analysed.

XRD confirms that part of the TiC powder is converted into anatase and rutile in the ratio of about 3:2 in the first peak and the remaining TiC, oxycarbide and anatase are converted into rutile in the second peak. The morphology of the 5 μm TiC powder at different stages of non-isothermal oxidation with a heating rate of 5°C min^{-1} in dry synthetic air is shown in Fig. 2. The starting TiC particles are irregularly shaped with sharp edges; see Fig. 2a. After oxidation up to 530 $^\circ\text{C}$, some anatase was formed at the surfaces; see Fig. 2b. Finally, after full transformation into rutile the particles became more rounded at the edges as shown in Fig. 2c.

As the experiment in Fig. 1 proceeded, the gases evolved were collected and analysed. CO_2 was the only gas detected, and the recorded pressure is

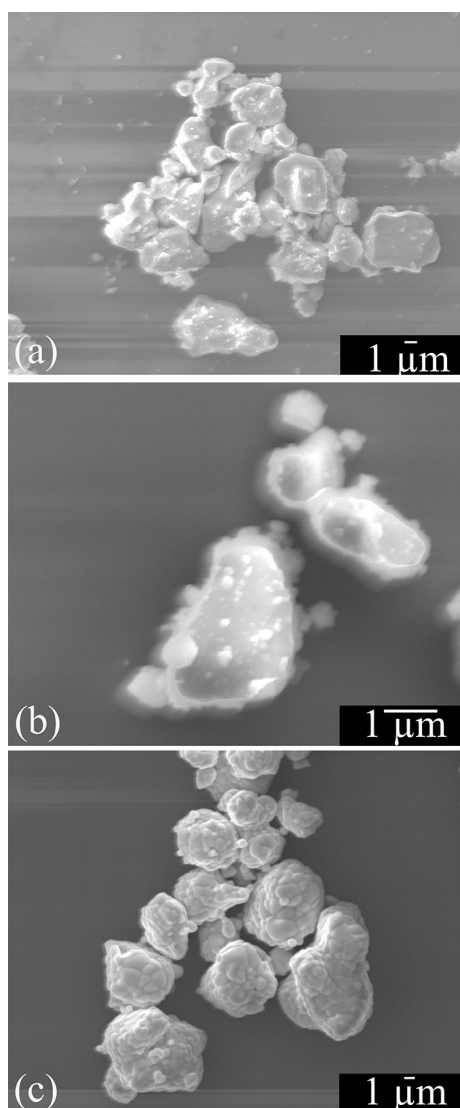


Figure 2 SEM images of TiC powder with an average particle size of 5 μm after non-isothermal oxidation in synthetic dry air with a heating rate of 5 $^{\circ}\text{C min}^{-1}$; cf. Fig. 1. **a** The raw powder, **b** oxidized up to 530 $^{\circ}\text{C}$ (formation of anatase) and **c** oxidised up to 1200 $^{\circ}\text{C}$ (fully transformed into rutile).

presented in Fig. 3. It is noticeable that the removal of C via CO_2 release and the precipitation of TiO_2 occur simultaneously as the heat flow peaks in Fig. 1 and the CO_2 signal in Fig. 3 closely overlap at the same temperatures.

A zoom in at about 320 $^{\circ}\text{C}$ of Fig. 3 shows a small peak (inset of Fig. 3) which is not immediately identified in the heat flow signal in Fig. 1. Hence, the mass change signal in Fig. 1 is further differentiated in Fig. 4, and then a kink coinciding with the peak at 320 $^{\circ}\text{C}$ in Fig. 3 is identified.

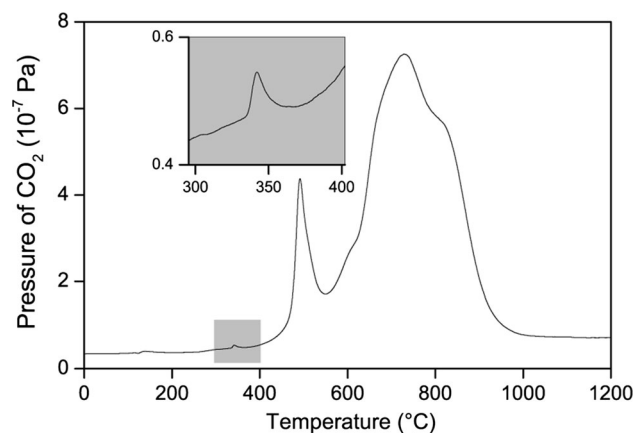


Figure 3 Evolution of CO_2 during oxidation of TiC powder with average particle size of 5 μm in dry synthetic air recorded with 5 $^{\circ}\text{C min}^{-1}$. Insert confirms the release of CO_2 during oxycarbide formation.

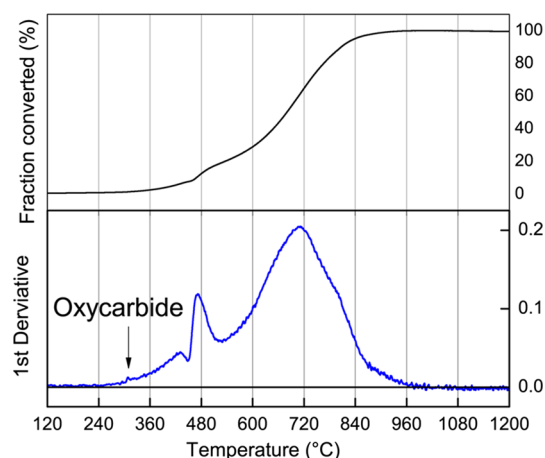


Figure 4 Differentiated mass gain signal ($d\Delta m/dt$) of 5 μm TiC powder recorded with 5 $^{\circ}\text{C min}^{-1}$ when oxidizing in dry synthetic air.

Another experiment using a fresh sample was run under the same conditions until 360 $^{\circ}\text{C}$ to determine the reaction occurring around 320 $^{\circ}\text{C}$. No oxide was identified by XRD after controlled cooling of the reaction product obtained although the sample weight had increased and CO_2 had been released. The combination of observations shows that the low-temperature peak is due to the substitution of atomic oxygen at carbon sites of the TiC lattice [12], leading to the formation of $\text{TiC}_y\text{O}_{1-y}$ which is evidenced by the reduction in the lattice parameter of TiC [24]. In this specific case, the lattice parameter of the starting material reduced from 4.3275 ± 0.0001 to 4.3260 ± 0.00005 \AA after heating up to 360 $^{\circ}\text{C}$. This oxycarbide phase exists throughout the oxidation

process [12, 25] and thus may act as a precursor for the formation of anatase and rutile.

The oxidation of the 5 μm powder can be summarized as follows. A first oxycarbide formation stage takes place over the interval from about 300–360 $^{\circ}\text{C}$. A second oxidation stage which leads to the formation of both rutile and anatase sets in after the first reaction and peaks around 470 $^{\circ}\text{C}$ and ends just before 530 $^{\circ}\text{C}$; see Fig. 1. (This stage is hereafter referred to as the anatase formation stage.) Although a single peak in the heat flow signal characterizes this step, the mass change signal clearly shows two consecutive stages. The first of these two stages starts from 430 to 470 $^{\circ}\text{C}$, and this proceeds relatively fast showing a very steep conversion versus temperature curve. The second stage which proceeds at a relatively slower rate continues from 470 $^{\circ}\text{C}$ and ends at about 520 $^{\circ}\text{C}$. A last oxidation stage starts from 530 $^{\circ}\text{C}$ and ends at around 960 $^{\circ}\text{C}$, where the remaining TiC, oxycarbide and anatase are converted into rutile. A similar reaction scheme was observed and reported earlier by [12] when studying the oxidation behaviour of TiC powder at various oxygen

partial pressures. However, in that study the second stage was split up into the formation of anatase and rutile; in addition, it was mentioned that these two stages may overlap and cannot be clearly distinguished from each other.

To continue, the other powders were all heated at 5 $^{\circ}\text{C min}^{-1}$ in air in separate experiments. The results are presented in Fig. 5. As observed for the 5 μm powder, multiple peaks are identified for the different particle sizes. The stages of oxidation were resolved by running separate experiments up to each identified peak in the heat flow or the differentiated mass change signal, and then the products were analysed by XRD and/or XMA.

For the coarsest powders having an average particle size of 140 and 48 μm , only the peaks pertaining to the formation of anatase and rutile can be identified in the heat flow and mass change signals (see Fig. 5a, b, respectively). The stage of oxycarbide formation appears to be overshadowed. For both powders, the peak occurring between 400 and 600 $^{\circ}\text{C}$ corresponds to the formation of anatase. The formation of rutile sets in at 800 $^{\circ}\text{C}$ and ends at 1195 $^{\circ}\text{C}$ for

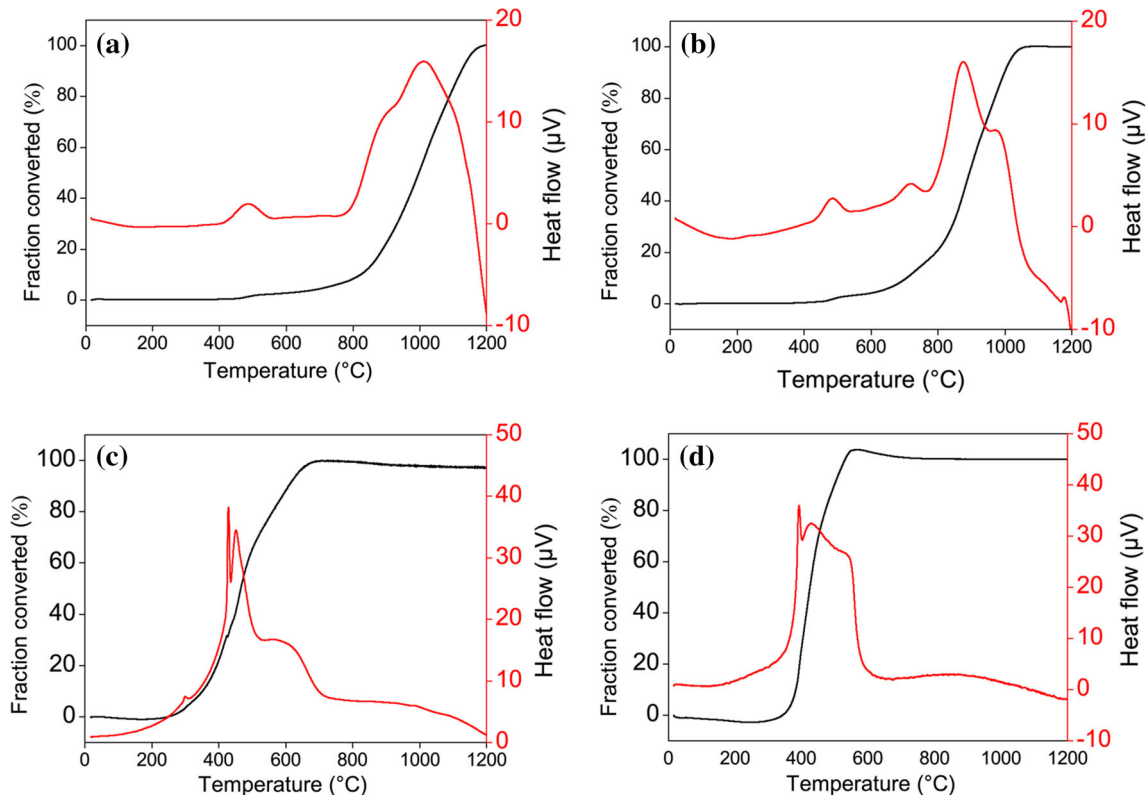


Figure 5 Heat flow and mass change in terms of converted fraction TiC (in %) as a function of temperature recorded at 5 $^{\circ}\text{C min}^{-1}$ in dry synthetic air of TiC powders with average size of: **a** 140 μm , **b** 48 μm , **c** 0.8 μm and **d** 0.05 μm .

the 140 μm powder, and for the 48 μm powder it starts from 700 $^{\circ}\text{C}$ and ends around 1050 $^{\circ}\text{C}$. It is noteworthy that the transformation into rutile of both coarse powders occurs via multiple steps while the mass gain signal for this range reflects a single peak event (i.e. a non-changing slope).

For the 0.8 μm TiC powder, all three stages observed for the 5 μm powder can be identified in the heat flow signal. The formation of the oxycarbide is shown in Fig. 5c peaking at about 310 $^{\circ}\text{C}$, as well as in the differentiated mass gain signals shown in Fig. 6. Anatase is formed in the sharp peak around 420 $^{\circ}\text{C}$ followed immediately by conversion into rutile which also occurs via two peaks.

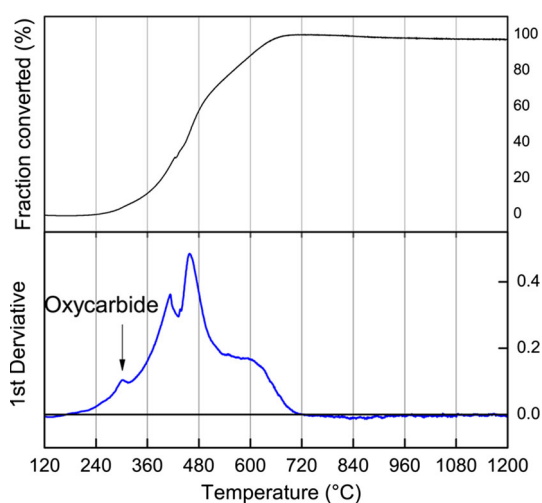


Figure 6 Differentiated mass gain signal ($d\Delta m/dt$) of 0.8 μm TiC powder recorded with 5 $^{\circ}\text{C min}^{-1}$ in dry synthetic air.

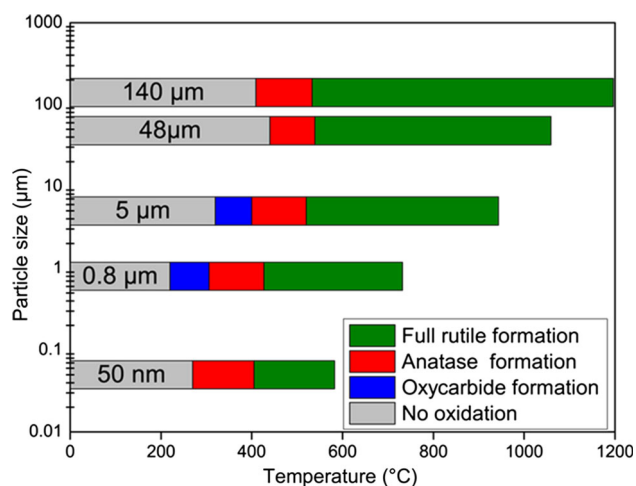


Figure 7 Chart showing the various stages of oxidation in dry synthetic air of TiC particles with different average particle sizes.

Figure 8 Heat flow and mass change in terms of converted fraction TiC (in %) as a function of temperature recorded at different heating rates in dry synthetic air of TiC powders with average particle size of: a, b 140 μm , c, d 48 μm , e, f 5 μm , g, h 0.8 μm and i, j 0.05 μm .

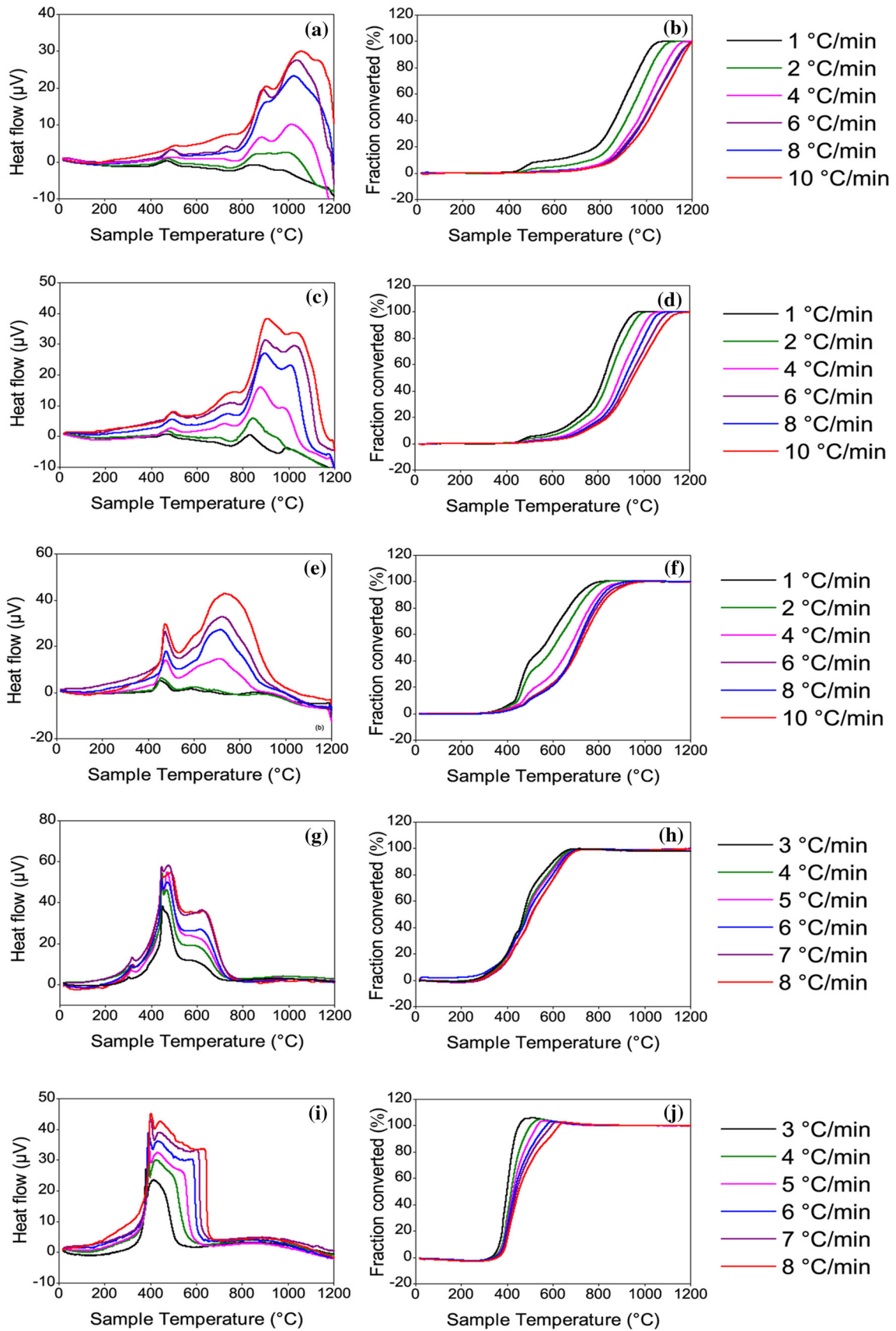
For the nano-powder the mechanism somewhat reverses to that of the coarser powders as no trace of the oxycarbide formation can be detected. A peak corresponding with the formation of anatase can be identified at 400 $^{\circ}\text{C}$, and two peaks associated with the formation of rutile can be identified at about 430 and 550 $^{\circ}\text{C}$, respectively, in Fig. 5d. The various stages of oxidation, as identified for the different particle sizes, are summarized as a function of temperature in Fig. 7. Depending on the particle size, some stages may overlap or is overshadowed and hence not always clearly resolved in the mass gain and heat flow signals as a function of temperature.

Effect of heating rate on oxidation

As the heating rate is increased, the amount of TiC transformed into anatase is reduced. For example, for the 140 μm powder the amount of TiC transformed decreases from 4 to 1% as heating rate is increased from 1 to 10 $^{\circ}\text{C min}^{-1}$. Similarly, there was a decrease of about 5–1.5% and 40–15% for the 48 and 5 μm powders, respectively, during the same stage, see Fig. 8.

For the same amount of powder, the surface area exposed to oxygen increases when the TiC particle size is reduced. Then, the conversion of TiC into TiO_2 is enhanced. This is evident from the heat flow signal recorded with the same heating rate, which increases for smaller particles. For example, the formation of rutile when oxidizing 5 μm TiC powder at 10 $^{\circ}\text{C min}^{-1}$ corresponds with about 45 μV of heat evolved, while under the same conditions 140 μm TiC powder results in about 28 μV of heat evolved; cf. Fig. 8a, e. Since the oxidation of TiC powder is faster when the particle size is smaller, the final temperature for full conversion of TiC powder into TiO_2 (rutile) during non-isothermal oxidation (at the same heating rate) decreases with particle size; see Fig. 8.

A final observable trend is that the stages of oxidation are well separated from each other (in both the heat flow and the fraction converted signals) at larger particle sizes. However, as the particle size is reduced, these stages become indistinguishable in the



fraction converted plots especially for the 50 nm powder.

Evaluation of the activation energy

The activation energy for oxidation of the different TiC powders is determined using Eq. (8). As more than one peak occurs during the transformation reaction, the peak temperature (T_p) is defined as the highest point in the differentiated mass gain signal. The results for the various TiC powders are presented in Fig. 9. With decreasing particle size, the lines for the maximum conversion of TiC into TiO₂ shifts to lower temperatures, and this defines the temperature window where a particle is activated. The slope of these lines corresponds to the activation energy of the reaction, and the figure clearly shows it decreases with decreasing particle size.

The values of the activation energy E_A as a function of the TiC particle size are presented in Table 2. It is observed that E_A significantly decreases with decrease in particle size for submicron and nano-sized particles and is more or less constant for particle sizes $> 5 \mu\text{m}$. The activation energies determined here are comparable to those determined in other studies (e.g. [11, 25]), i.e. 192 and 245 kJ mol⁻¹. The (non-significant) difference may arise from the size of the TiC particles and the limited temperature window of the isothermal experiments used in the present analysis.

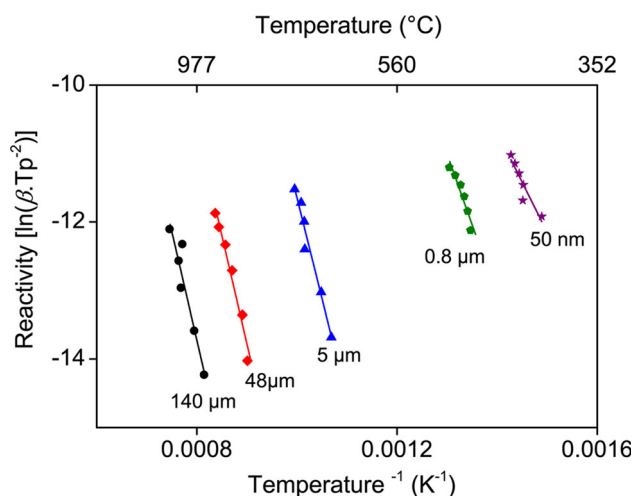


Figure 9 Kissinger plot for estimating the activation energies size for the oxidation of TiC powder with different particles sizes in dry synthetic air; see Eq. (8).

Table 2 Activation energies as determined for oxidation of TiC powders with different particle sizes

Size (μm)	E_A (kJ mol ⁻¹)
140	263 \pm 42
48	262 \pm 23
5	244 \pm 24
0.8	172 \pm 27
0.05	122 \pm 24

Effects of particle size on the activation energy have been reported for other materials as well [26, 27]. It can be conceived that when the surface-to-volume ratio increases the activation energy decreases, since the atoms at the surface have fewer bonds and neighbouring atoms and thus need less energy to transfer into oxide [28].

Hence, the reduction of the bulk activation energy, E_A^{bulk} , can be related to the surface energy σ according to [29]:

$$E_A = E_A^{\text{bulk}} - \frac{6\sigma V_m}{d} \quad (15)$$

in which V_m is the molar volume and d the particle size. For TiC the surface energy equals 2.73 J m⁻² [30] and the molar volume 12.18 cm³ mol⁻¹ [31]. From Fig. 10, the observed reduction in the activation energy for submicron or nano-sized particles is due to surface defects (like: dislocations, grain boundaries, steps and kinks, roughness), of which their number increases with surface area (i.e. with d^{-2}) [32]. These surface defects promote the nucleation and growth of the oxide.

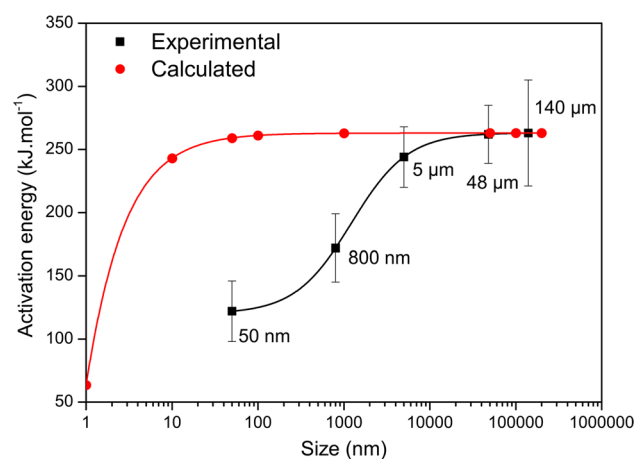
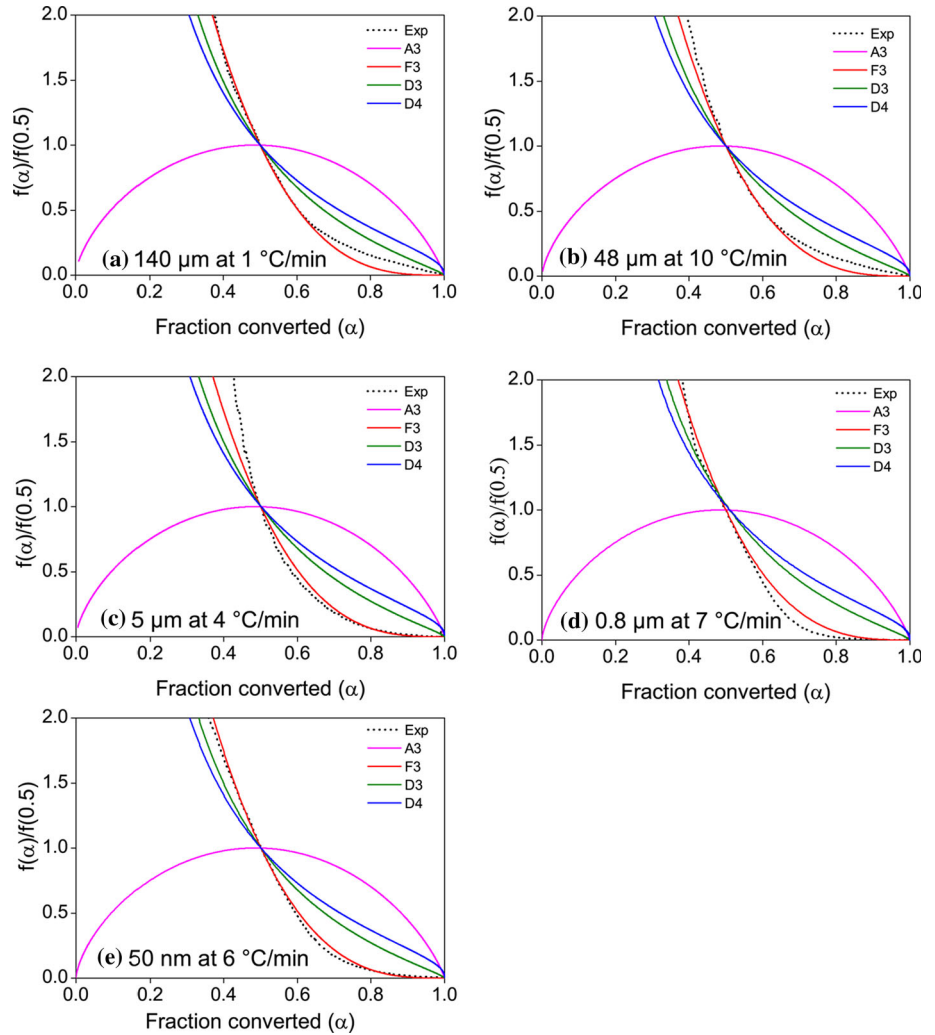


Figure 10 Activation energy as a function of particle size for the oxidation of TiC powder in dry synthetic air. The calculated values pertain to the effect of surface-to-volume ratio; see Eq. (15).

Figure 11 Master plots of theoretical models and experimental data of TiC powders with average size of: **a** 140 μm, **b** 48 μm, **c** 5 μm, **d** 0.8 μm and **e** 0.05 μm.



Hence, the activation energy as a function of particle size is presented in Fig. 10 and the relationship can be best described with Eq. (16).

$$E_A = 263 + \left(\frac{120 - 263}{\left(1 + \left(\frac{d}{1220}\right)^{1.325}\right)} \right) \quad (16)$$

where E_A is the activation energy in kJ mol^{-1} and d is the particle size in nm.

Reaction model for TiC oxidation

Out of the many reaction models [18], the non-isothermal plots of the rate of conversion with temperature pre-empt that the oxidation of TiC may be either an Avrami-Erofev, diffusion, or an order reaction model. Hence, the experimental data are compared with the Avrami-Erofev (A3), 3D

diffusion Jander (D3), Ginstling-Brounshtein (D4) and the third-order (F3) reaction models using the master curve plotting method [23]; see “Reaction model” section. To ascertain the validity of the identified model, master plots are made for all the powders at different heating rates, see Fig. 11. It is seen that for different heating rates the experimental data closely resemble the F3 (third-order reaction model) more than any other model. The integral and the differential form of the third-order reaction model is, respectively, defined as:

$$g(\alpha) = (1/2) \left[(1 - \alpha)^{-2} - 1 \right] \quad (17)$$

$$f(\alpha) = (1 - \alpha)^3 \quad (18)$$

The rate-determining step in the oxidation of TiC is the diffusion of oxygen from the gaseous phase through the formed oxide layers and the opposite

Table 3 Evaluated pre-exponential factors (A) for TiC powders oxidized in dry synthetic air

Size (μm)	A (s^{-1})
140	3.3×10^{10}
48	5×10^{10}
5	100×10^{10}
0.8	8.3×10^{10}
0.05	1×10^8

diffusion of titanium and carbon from the material into the scale.

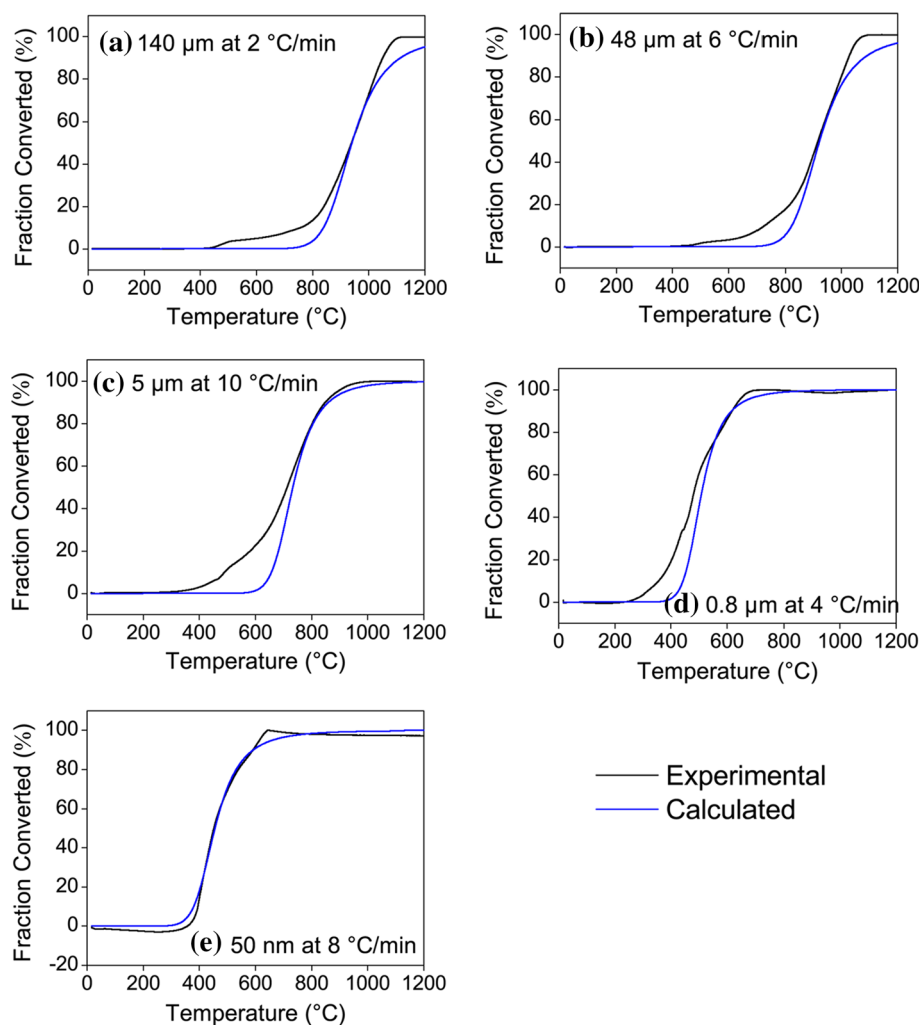
The Arrhenius pre-exponential factor

The last of the kinetic triplet, i.e. the pre-exponential factor (A), is evaluated from the integral form of the kinetic rate equation given in Eq. (11) combined with Eq. (17). The generalized time Eq. (9) is determined at every temperature from 25 to 1200 °C using

Eq. (14), the applied heating rate and the estimated E_A . A linear fitting of Eq. (11) is made for the range of α pertaining to the third oxidation stage (i.e. transformation into rutile) to find the constant A . The calculated pre-exponential factors, as shown in Table 3, are relatively constant with the same order of magnitude. However, it significantly decreases for the nanometre-sized particles [33, 34]. As the particle size decreases, the partial molar surface enthalpy and the partial molar surface entropy increase, leading to the decrease in the apparent activation energy and the pre-exponential factor [29, 35]. There is no simple explanation for the high value of the Arrhenius parameter for the 5 μm particle, other than undetected impurities or structural defects.

Finally, the conversion α of TiC into TiO_2 by oxidation in air can be expressed as a function of temperature and time for each particle size by:

Figure 12 Comparing the fraction converted (α) for the experimental data and the calculated results of TiC powders in dry synthetic air.



$$\alpha = 1 - [(2A\theta + 1)^{-1/2}] \quad (19)$$

with θ calculated using Eq. (14). It can be seen in Fig. 12 that at higher temperatures the calculated results fit well with the experimental results with a slight deviation at lower temperatures. This deviation is associated with initial stages of oxidation which corresponds to the formation of the oxycarbides and/or anatase.

Conclusions

Oxidation of TiC was found to proceed via the formation of oxycarbides \rightarrow anatase/rutile \rightarrow rutile and closely follows a third-order reaction path. The temperature window for activation of the oxidative decomposition of the TiC healing particles, i.e. for triggering the self-healing reaction, drops from 1000 to 400 °C as particle size decreases from 140 μm to 50 nm. As the change in optimal healing temperature does not depend on the chemical composition of the matrix material as such, the present study shows in a generic manner that extrinsic self-healing in oxide ceramic matrices can be tailored to a specific temperature range by tuning the size of the healing particle. Further, the activation energy required for oxidation decreases significantly for particles ranging between 10 μm to 50 nm. Above 10 μm particle size, the activation energy for the thermal oxidation of TiC becomes constant.

Acknowledgements

This research was sponsored by the People Program (Marie Curie ITN) of the European Union's seventh framework programme, FP7, Grant No. 290308 (SHeMat). The authors are indebted to Ing. Ruud Hendriks for performing XRD analysis.

Open Access This article is distributed under the terms of the Creative Commons Attribution 4.0 International License (<http://creativecommons.org/licenses/by/4.0/>), which permits unrestricted use, distribution, and reproduction in any medium, provided you give appropriate credit to the original author(s) and the source, provide a link to the Creative Commons license, and indicate if changes were made.

References

- [1] Yoshioka S, Boatema L, van der Zwaag S, Nakao W, Sloof WG (2016) On the use of TiC as high-temperature healing particles in alumina based composites. *J Eur Ceram Soc* 36(16):4155–4162. <https://doi.org/10.1016/j.jeurceramsoc.2016.06.008>
- [2] Boatema L, Kwakernaak C, van der Zwaag S, Sloof WG (2016) Selection of healing agents for autonomous healing of alumina at high temperatures. *J Eur Ceram Soc* 36(16):4141–4145. <https://doi.org/10.1016/j.jeurceramsoc.2016.05.038>
- [3] Ando K, Kim BS, Chu MC, Saito S, Takahashi K (2004) Crack-healing and mechanical behaviour of $\text{Al}_2\text{O}_3/\text{SiC}$ composites at elevated temperature. *Fatigue Fract Eng Mater Struct* 27(7):533–541. <https://doi.org/10.1111/j.1460-2695.2004.00785.x>
- [4] Osada T, Nakao W, Takahashi K, Ando K, Saito S (2007) Strength recovery behavior of machined $\text{Al}_2\text{O}_3/\text{SiC}$ nanocomposite ceramics by crack-healing. *J Eur Ceram Soc* 27(10):3261–3267. <https://doi.org/10.1016/j.jeurceramsoc.2006.11.080>
- [5] Ono M, Nakao W, Takahashi K, Nakatani M, Ando K (2007) A new methodology to guarantee the structural integrity of $\text{Al}_2\text{O}_3/\text{SiC}$ composite using crack healing and a proof test. *Fatigue Fract Eng Mater Struct* 30(7):599–607
- [6] Ando K, Chu MC, Yao F, Sato S (1999) Fatigue strength of crack-healed $\text{Si}_3\text{N}_4/\text{SiC}$ composite ceramics. *Fatigue Fract Eng Mater Struct* 22(10):897–903. <https://doi.org/10.1046/j.1460-2695.1999.00210.x>
- [7] Salas-Villaseñor AL, Lemus-Ruiz J, Nanko M, Maruoka DM (2009) Crack disappearance by high-temperature oxidation of alumina toughened by Ni nano-particles. *Adv Mater Res* 68:34–43
- [8] Nakao W, Abe S (2012) Enhancement of the self-healing ability in oxidation induced self-healing ceramic by modifying the healing agent. *Smart Mater Struct* 21:1–7
- [9] Farle A, Boatema L, Shen L, Gövert S, Kok JBW, Bosch M, Yoshioka S, Svd Zwaag, Sloof WG (2016) Demonstrating the self-healing behaviour of some selected ceramics under combustion chamber conditions. *Smart Mater Struct* 25(8):084019
- [10] Lavrenko VA, Glebov LA, Pomitkin AP, Chuprina VG, Protsenko TG (1975) High-temperature oxidation of titanium carbide in oxygen. *Oxid Met* 9(2):171–179. <https://doi.org/10.1007/bf00613231>
- [11] Stewart RW, Cutler IB (1967) Effect of temperature and oxygen partial pressure on the oxidation of titanium carbide. *J Am Ceram Soc* 50(4):176–181. <https://doi.org/10.1111/j.1151-2916.1967.tb15076.x>

- [12] Shimada S (1996) A thermoanalytical study of oxidation of TiC by simultaneous TGA-DTA-MS analysis. *J Mater Sci* 31:673–677. <https://doi.org/10.1007/BF00367884>
- [13] Shimada S, Kozeki M (1992) Oxidation of TiC at low temperatures. *J Mater Sci* 27(7):1869–1875. <https://doi.org/10.1007/BF01107214>
- [14] Favergeon L, Morandini J, Pijolat M, Soustelle M (2013) A general approach for kinetic modeling of solid-gas reactions at reactor scale: application to Kaolinite Dehydroxylation. *Oil Gas Sci Technol—Rev IFP Energies Nouvelles* 68(6):1039–1048
- [15] Turkdogan ET (1977) Gas-solid reactions, J. Szekely, J. W. Evans and H. Y. Sohn, Academic Press, 1976. 400 pages. *AIChE J* 23(4):612–612. <https://doi.org/10.1002/aic.690230435>
- [16] Xu Z, Sun X, Khaleel MA (2012) A generalized kinetic model for heterogeneous gas-solid reactions. *J Chem Phys* 137(7):074702
- [17] Brown EM (2001) Introduction to thermal analysis: techniques and applications, introduction to thermal analysis: techniques and applications, 2nd edn. Kluwer, Amsterdam. <https://doi.org/10.1007/0-306-48404-8>
- [18] Khawam A, Flanagan DR (2006) Solid-state kinetic models: basics and mathematical fundamentals. *J Phys Chem B* 110(35):17315–17328. <https://doi.org/10.1021/jp062746a>
- [19] Lyon RE (1997) An integration method of non-isothermal kinetic analysis. Federal aviation administration, U.S. Department of transportation
- [20] Senum GI, Yang RT (1977) Rational approximations of the integral of the Arrhenius function. *J Therm Anal* 11(3):445–447. <https://doi.org/10.1007/bf01903696>
- [21] Kissinger HE (1957) Reaction kinetics in differential thermal analysis. *Anal Chem* 29(11):1702–1706. <https://doi.org/10.1021/ac60131a045>
- [22] Kissinger HE (1956) Variation of peak temperature with heating rate in differential thermal analysis. *J Res Natl Bureau Stand* 57(4):217–221
- [23] Gotor FJ, Criado JM, Malek J, Koga N (2000) Kinetic analysis of solid-state reactions: the Universality of Master plots for analyzing isothermal and nonisothermal experiments. *J Phys Chem A* 104(46):10777–10782. <https://doi.org/10.1021/jp0022205>
- [24] Sloof WG, Delhez R, de Keijser TH, Schalkoord D, Ramaekers PPJ, Bastin GF (1988) Chemical constitution and microstructure of TiC x coatings chemically vapour deposited on Fe–C substrates; effects of iron and chromium. *J Mater Sci* 23(5):1660–1672. <https://doi.org/10.1007/bf01115705>
- [25] Voitovich VB (1997) Mechanism of the high temperature oxidation of titanium carbide. *High Temp Mater Process* (London). <https://doi.org/10.1515/HTMP.1997.16.4.243>
- [26] Kurlov AS, Gusev AI (2011) Effect of particle size on the oxidation of WC powders during heating. *Inorg Mater* 47(2):133–138. <https://doi.org/10.1134/s0020168511020099>
- [27] Quanli J, Haijun Z, Suping L, Xiaolin J (2007) Effect of particle size on oxidation of silicon carbide powders. *Ceram Int* 33(2):309–313. <https://doi.org/10.1016/j.ceramint.2005.09.014>
- [28] Phuoc TX, Chen R-H (2012) Modeling the effect of particle size on the activation energy and ignition temperature of metallic nanoparticles. *Combust Flame* 159(1):416–419. <https://doi.org/10.1016/j.combustflame.2011.07.003>
- [29] Fu Q-S, Xue Y-Q, Cui Z-X, Wang M-F (2014) Study on the size-dependent oxidation reaction kinetics of nanosized zinc sulfide. *J Nanomater* 2014:8. <https://doi.org/10.1155/2014/856489>
- [30] Hugosson HW, Eriksson O, Jansson U, Ruban AV, Souvatzis P, Abrikosov IA (2004) Surface energies and work functions of the transition metal carbides. *Surf Sci* 557(1):243–254. <https://doi.org/10.1016/j.susc.2004.03.050>
- [31] Villars P, Cenzual K (eds) (2010) Pearson's crystal data-crystal structure database for inorganic compounds. ASM International, Materials Park, Ohio, USA
- [32] Šesták J (2011) Rationale and fallacy of thermoanalytical kinetic patterns. *J Therm Anal Calorim* 110(1):5–16. <https://doi.org/10.1007/s10973-011-2089-1>
- [33] Zhang W, Xue Y, Cui Z (2017) Size-dependence of surface thermodynamic functions of nano-Cu by dissolution kinetics. *Colloids Surf A* 533:81–86. <https://doi.org/10.1016/j.colsurfa.2017.07.064>
- [34] Cui Z, Duan H, Xue Y, Li P (2015) An investigation of the general regularity of size dependence of reaction kinetics of nanoparticles. *J Nanopart Res*. <https://doi.org/10.1007/s11051-015-3017-2>
- [35] Fu Q, Cui Z, Xue Y (2015) Size dependence of the thermal decomposition kinetics of nano-CaC₂O₄: a theoretical and experimental study. *Eur Phys J Plus*. <https://doi.org/10.1140/epjp/i2015-15212-4>